Continuous wavelet-like filter for a spherical surface and its application to localized admittance function on Mars.

*Motoyuki Kido[1], David A. Yuen[2], and Alain P. Vincent [3]

[1] JSPS, Domestic Res. Fellow at JAMSTEC
Natsushima-cho 2-15, Yokosuka-shi, 237-0061, Japan
(kido@jamstec.go.jp)
Tel: +81-468-67-9329, Fax: +81-468-67-9315

[2] Department of Geology and Geophysics and Minnesota Supercomputer Institute
University of Minnesota
Minneapolis, MN 55455-0219, U.S.A.
(davey@krissy.geo.umn.edu)

[3] Département de Physique, Université de Montréal,
H3C 3J7, Montréal, Québec, Canada
(vincent@astro.umontreal.ca)

submitted to *Phys. Earth Planet. Inter.*, October, 2001,
revised, August, 2002

Key words: wavelet, bandpass filter, Martian gravity data, admittance

The manuscript contains **7800** words and **16** equations.

* corresponding author

Abstract. We have developed a 2D isotropic continuous wavelet-like transform for a spherical surface. The transform is simply defined as the surface convolution between the original field and a kernel, based on the zeroth-order Bessel function with a spherical correction. This spherical correction violates the geometric similarity for the various scales of the kernels, which becomes more apparent at longer wavelengths. We found numerically that this transform is practically equivalent to a Gaussian bandpass filter in the spherical harmonic domain. We have applied this wavelet-like transform on the recently acquired Martian gravity and topography fields. Using a ratio constructed locally from these two fields, we have constructed a map describing the lateral variations of the localized admittance function on Mars.

1 Introduction

The analysis of the gravity and the topography of planetary bodies, such as Venus, Mars and the Moon, provides valuable information about the dynamical behavior of their mantles and the thermomechanical state of their lithospheres. Classical spectral analysis on these data using the spherical harmonics gives a globally averaged quantity. However, in the course of studying the lateral variations of the physical properties, such as the crustal and lithospheric thicknesses, we will need to know the local spatial information as well as the wavelength content. In actuality, a fully spectral analysis, confined within a selected region, is a common approach for localizing features manually (McKenzie et al., 2002). Wavelet transform is a powerful mathematical tool for spatially localized spectral studies, which has been widely employed in the solid Earth community (Kumar and Foufoula-Georgiou, 1997; Simons et al., 1997; Gibert et al., 1998; Moreau et al., 1999; Bergeron et al., 1999, 2000; Guyodo et al., 2000; Chiao and Kuo, 2001; Vecsey and Matyska, 2001; Piromallo et al., 2001;

Yuen et al., 2002).

In regional studies, the Cartesian approximation (Piromallo et al., 2001) is realistic and even one dimensional analyses (McNutt and Parker, 1978; Malamud and Turcotte, 2001; McKenzie et al., 2002; Turcotte et al., 2002) are useful for quantifying lineated structures, often appearing on planetary surfaces. On the other hand, we need to consider the full spherical geometry for large-scale lateral variation of the data field. In recent years there have been some fundamental works carried out by applied mathematicians on extending the wavelet concept to spherical geometry (Narcowich and Ward, 1996; Freeden and Windheuser, 1996, 1998; Li, 1999; Antoine et al., 2002) for both continuous and discrete wavelet transforms. The algorithms developed in these studies are cast in a mathematical framework difficult for most geophysicists to comprehend and to employ in their own investigations. Therefore, we have sought to develop a simpler way of looking at spherical wavelet-like transform, which can be constructed easily by geophysicists in order to promote the use of wavelets in our field. Our approach is analytical in character and the wavelet kernel is based on the zeroth-order Bessel function, which is derived by the azimuthal averaging of the well-known anisotropic Gabor transform (Daugman, 1985). We call this transform as "wavelet-like", since the kernel has been adjusted with a spherical correction, which consequently breaks the geometric similarity of the various scales in the kernels.

Recently, the Mars Global Surveyor mission (Zuber et al., 1992) provides high resolution geodetic data (Smith et al, 1999a, 1999b, 2001; Yuan et al, 2001). The satellite altimetry tracking (MOLA: Martian Orbiter Laser Altimeter) yields quite fine scale topographic mapping with a uniform resolution up to 0.15625 arc degree (Smith et al., 1999b). On the other hand, the gravitational potential data is based on the X band tracking data. Thus the resolution of the Martian gravity data is up to only 80 degree at most in spherical harmonics (Lemoine et al., 2001). However, this

corresponds to a resolution of about 133 km in the half-wavelength for the smaller Martian radius. The thickness of the mechanical lithosphere may be comparable to that of the Earth (McKenzie et al., 2002; Turcotte et al., 2002) and is of the same order of the resolution of the data. Therefore, it has a great potential for providing significant information on the mechanical state of the Martian lithosphere at least where the lithosphere is thickest.

In practice, these data have been used to elucidate Martian crustal and lithospheric structures (Smith et al., 1999c; Zuber et al., 2000; McGovern et al., 2000; Zuber, 2001; Arkani-Hamed, 2000; McKenzie et al., 2002).

In this work we present a simple algorithm for constructing a wavelet-like transform on a sphere, and apply this formulation to Martian gravity and topography fields. Then we compare the transform with a bandpass filter in the spectral domain cast in terms of the traditional spherical harmonics representation in order to clarify the nature of the transform. Next we construct the ratio of gravity to topography (the admittance function) over the spherical surface, which is simultaneously localized in the two quantities, space and wavelength, and then examine the balance of localization between these two antithetical quantities. Finally we consider the geophysical implications of the lateral variations of the Martian lithospheric structure with a map depicting the localized admittance function.

2 Kernel of a wavelet-like transform on the sphere

We will now describe the construction of an analytical wavelet-like transform, which can be applied over the spherical surface. This approach is different from the bandwidth filter method based on spherical harmonics and Wigner 3-j formalism by Simons et al. (1977). It is well known that the minimum mathematical requirements to be

satisfied by a mother wavelet (e.g., Daugman, 1985) are: (1) the mean of the wavelet function over the entire interval is zero; (2) the geometric similarity must be kept over the different spatial scales. By satisfying these conditions simultaneously, we have then two types of wavelet transforms, the continuous wavelet transform (CWT) and the discrete wavelet transform (DWT). If the mother wavelet is orthogonal over the discrete wavelengths, then it takes the form of the DWT, which can reconstruct the original field with a minimum transformed data set over the discrete scales (Mallat, 1998). This approach works well for digital image compression and the archiving of large data sets. On the other hand, CWT contains redundant information in the transformed data set, but can define the transform at any arbitrary wavelength, which is extremely useful for spectral analysis of continuous geophysical data fields.

In general, a two-dimensional isotropic wavelet transform is calculated by combining one-dimensional transforms along both the x and y axes, in the same manner as the 2D Fast Fourier Transform (FFT), which can immensely speed up the computations (Bergeron et al., 1999). In this study we will not follow such a task but rather employ a direct 2D transform according to the definition of the wavelet transform, namely a convolution of a kernel with the original field over the surface. Our purpose is to clarify more the physical meaning with a detailed analytical treatment, rather than to speed up the computation and to lose some physical insight in the process.

As a first step, we will employ the Gabor transform, based on Fourier analysis with a Gaussian window. The Gabor transform has a long and rich history (Gabor, 1946). The kernel of the one-dimensional Gabor transform $F1_{k,\sigma}(x)$ is one of the more popular mother wavelets, which is used for time-series analysis (Folland, 1989). It simply consists of three parts; $\exp(-(kx/(2\sigma))^2)$ as a Gaussian window, and $\cos kx$ as a basis function subtracted by a constant $\exp(-\sigma^2)$ to insure that the mean value

of the kernel to be zero.

$$F1_{k,\sigma}(x) = \exp\left(-\left(\frac{kx}{2\sigma}\right)^2\right)\left[\cos kx - \exp(-\sigma^2)\right], \tag{1}$$

where k is a wavenumber and σ/k is the width of the Gaussian window along the x direction. We note that the window size is variable and is proportional to the wavelength to be considered. It can also play an important role in offering an optimal resolution, to be discussed later.

The kernel of the two-dimensional anisotropic Gabor transform in Cartesian geometry $Fa_{k,\sigma}(x,y)$ (Fig. 1a) is also popular and is mainly applied to the pattern recognition of 2D images (Daugman, 1985). It is defined by extending $\cos kx$ in Eq. 1 in the y direction as a constant (Fig. 1c) with the zero-mean adjustment term and the 2D Gaussian window (Fig. 1b);

$$Fa_{k,\sigma}(x,y) = \exp\left(-\left(\frac{k\sqrt{x^2+y^2}}{2\sigma}\right)^2\right)\left[\cos kx - \exp\left(-\sigma^2\right)\right]. \tag{2}$$

Eq. 2 can also be rewritten in the cylindrical coordinate system as:

$$Fa_{k,\sigma}(r,\psi) = \exp\left(-\left(\frac{kr}{2\sigma}\right)^2\right)\left[\cos(kr\cos\psi) - \exp\left(-\sigma^2\right)\right], \tag{3}$$

where r is a distance between the kernel center and a point at (x,y), and ψ is the azimuthal angle of the point from the x-axis.

Here, we define a new isotropic (axisymmetric) kernel $Fi_{k,\sigma}(r)$ (Fig. 1d) as an azimuthal average of $Fa_{k,\sigma}(r,\psi)$;

$$Fi_{k,\sigma}(r) = \frac{1}{2\pi}\int_0^{2\pi} Fa_{k,\sigma}(r,\psi)d\psi$$

$$= \frac{1}{2\pi}\exp\left(-\left(\frac{kr}{2\sigma}\right)^2\right)\left[\int_0^{2\pi}\cos(kr\cos\psi)d\psi - 2\pi\exp\left(-\sigma^2\right)\right]$$

$$= \exp\left(-\left(\frac{kr}{2\sigma}\right)^2\right)\left[J_0(kr) - \exp\left(-\sigma^2\right)\right], \tag{4}$$

where J_0 is the Bessel function of the zeroth-order. We note that $Fi_{k,\sigma}(r)$ is not an azimuthal integral of $Fa_{k,\sigma}(r,\psi)$, such as $(\int_0^{2\pi} Fa_{k,\sigma}(r,\psi)rd\psi)$. $Fi_{k,\sigma}(r)$ still keeps its mean value to be zero.

In order to map this 2D Cartesian kernel onto a spherical surface, we have to apply a spherical correction $\xi/\sin\xi$ to the basis function, where ξ is an angular distance instead of r in Eq. 4. This enforces the zero-mean criterion even on the sphere. In addition, we use a normalizing factor ℓ_w^2, where ℓ_w, instead of k, is the wavenumber on sphere corresponding to angular degree of the spherical harmonics. This normalization is important for generating an equivalent bandpass filter in the spherical harmonics, to be considered in a later section. Finally, the Gabor-type transform kernel for a sphere used in this study, $F_{\ell_w,\sigma}(\xi)$, can be expressed as;

$$F_{\ell_w,\sigma}(\xi) = \ell_w^2 \exp\left(-\left(\frac{\ell_w \xi}{2\sigma}\right)^2\right)\left[J_0(\ell_w\xi)\frac{\xi}{\sin\xi} - \exp\left(-\sigma^2\right)\right]. \tag{5}$$

ξ is also expressed by geographical system using ϕ_0, θ_0, ϕ, and θ, where (ϕ_0,θ_0) are longitude and co-latitude at a location to be considered for the transform (the central location of the kernel) and (ϕ,θ) is any geographical location. Since ξ is the angular distance along a great circle between (ϕ_0,θ_0) and (ϕ,θ),

$$\cos\xi = \cos\theta_0\cos\theta + \sin\theta_0\sin\theta\cos(\phi_0-\phi), \tag{6}$$

$F_{\ell_w,\sigma}(\xi)$ can be expressed also as $F_{\ell_w,\sigma,\phi_0,\theta_0}(\phi,\theta)$ in the geographic system. ℓ_w/σ is proportional to the window size, and σ is a key parameter which controls the balance of localization between space and wavelength. We have tested several cases with σ ranging from 2 to 8 in this study. There are also other types of spherical Gabor transforms developed by mathematicians in terms of other functions (e.g., Freeden and Schreiner, 1995).

Fig. 2a shows the vertical cross section of the kernel for the case of $\ell_w = 8$ and $\sigma = 2$. Firstly, the dotted line is the Bessel function in Eq. 5. With the spherical

correction, the undulation is amplified with increasing ξ (the short dotted line). The contribution of the mean value adjustment (denoted DC) is relatively small (the long dashed line). Finally by applying the window, the function becomes the curve represented by the solid line, which is very close to the condition for compact support. The normalizing term is omitted and the amplitude at $\xi = 0$ is unity in this figure.

By introducing the spherical correction, the shape of the kernel $F_{\ell_w,\sigma}(\xi)$ will be different, depending on ℓ_w, which violates one of the mathematical requirement for mother wavelet, namely the geometric similarity among the different scales. Fig. 2b demonstrates how the difference in $F_{\ell_w,\sigma}(\xi)$ depends on ℓ_w. Cases for $\ell_w = 2$, 3, 4, 5, 8, and 16 are shown for comparison. For evaluating the geometrical similarity, we have scaled the angular distance ξ by multiplying with $\ell_w/4$. A prominent feature is a singularity originated in the spherical correction for $\ell_w = 2$, 3, and 4 corresponding to the antipodes of the center of the kernel. The effective area of this singular point is infinitesimal so that the convolution over the sphere (described in next section) is stable and the criterion of zero-mean is preserved. In addition, due to the window, this singular point is not included in the actual convolution area for $\ell_w \geq 4$. The problem lies in the difference of the kernels around the scaled angular distance is 60°. However, we cannot observe any noticeable difference for $\ell_w \geq 8$ from the figure. Therefore the kernel defined here is not a mother wavelet in the strict mathematical sense but can be considered numerically to be a mother wavelet for $\ell_w \geq 8$. For this reason we have called our transform a "wavelet-like transform" and use the word "kernel" rather than the word "mother wavelet".

3 Spherical wavelet-like transform

We employed the Martian gravity G and topography T as the original data to be analyzed. These are made available to us as products of the Mars Global Surveyor mission, given by spherical harmonic coefficients up to degree 80 and 90, respectively. They are denoted in the spatial domain by the longitude ϕ and co-latitude θ as $G(\phi, \theta)$ and $T(\phi, \theta)$, respectively. A detailed description of the data will be presented later in the section dealing with the admittance function. In this section we take the topography data as an example of the transform.

The wavelet transform is defined to be the convolution between the mother wavelet (kernel) and the original field. Then the transformed field $\tilde{T}$, denoted with a tilde, at a geographic location (ϕ_0, θ_0) using the kernel defined in Eq. 5, can be written as

$$\tilde{T}_{\ell_w,\sigma}(\phi_0, \theta_0) = \frac{1}{4\pi} \int_0^{2\pi} \int_0^{\pi} T(\phi, \theta) F_{\ell_w,\sigma,\phi_0,\theta_0}(\phi, \theta) \sin\theta d\theta d\phi, \tag{7}$$

which is illustrated in Fig. 3. One only have to integrate Eq. 7 within $\xi < 2e\sigma/\ell_w$, where e is the base of the natural logarithms, which is 78° for the case in Fig. 2a. This is due to the fact that the kernel is close to having compact support ($F_{\ell_w,\sigma,\phi_0,\theta_0} \approx 0$ for $\xi > 2e\sigma/\ell_w$), as is clear in Figs. 2a and 2b. For $\sigma = 2$, $2e\sigma/\ell_w$ is greater than π when $\ell_w = 2$. In this case, some regions close to the antipodes of center of the kernel must be integrated twice in order to keep the kernel zero mean. This makes the physical meaning unclear. However, such a case occurs only at the longest wavelength, which is not of our interest for the admittance analysis.

The original and the transformed fields are shown in Fig. 7 in the later section, so that it can be directly compared with the admittance map discussed later.

4 Bandpass filter in spherical harmonics

The original field $T(\phi, \theta)$ and the transformed field $\tilde{T}_{\ell_w,\sigma}(\phi, \theta)$ can be expanded in spherical harmonics and are represented by sets of coefficients, $T_{\ell,m}$ and $\tilde{T}_{\ell_w,\sigma,\ell,m}$, respectively. We employed the fully-normalized spherical harmonic function, denoted by $Y_{\ell,m}(\phi, \theta)$ with angular degree ℓ and order m, whose normalization convention is described in Stacey (1992).

Here we can define the cross-correlation $C_{\ell_w,\sigma}(\ell)$ for each individual degree ℓ between the original and transformed fields in spectral domain, using the spherical harmonics coefficients $T_{\ell,m}$ and $\tilde{T}_{\ell_w,\sigma,\ell,m}$;

$$C_{\ell_w,\sigma}(\ell) = \frac{\sum_{m=-\ell}^{\ell} T_{\ell,m}\tilde{T}_{\ell_w,\sigma,\ell,m}}{\sqrt{\sum_{m=-\ell}^{\ell} T_{\ell,m}^2 \sum_{m=-\ell}^{\ell} \tilde{T}_{\ell_w,\sigma,\ell,m}^2}} \tag{8}$$

Fig. 4 shows the correlation $C_{\ell_w,\sigma}(\ell)$ for ℓ_w =2 to 64. $C_{\ell_w,\sigma}(\ell)$ is nearly unity for any degree ℓ. We only show $\ell \leq 2\ell_w$. Actually $C_{\ell_w,\sigma}(\ell)$ scatters at higher ℓ. However, the amplitude of $\tilde{T}_{\ell_w,\sigma,\ell,m}$ is almost zero at $\ell > 2\ell_w$ so that the scattering in $C_{\ell_w,\sigma}(\ell)$ may be a slight numerical inaccuracy of the calculation in Eq. 7 and can be neglected. We have confirmed that $C_{\ell_w,\sigma}(\ell)$ is nearly unity at any ℓ for all the selected ℓ_w. This demonstrates that the wavelet-like transform is numerically equivalent to some kind of filtering in the spectral domain, using the spherical harmonics. Therefore we can consider hereafter only the RMS (Root Mean Square) amplitude of $\tilde{T}_{\ell_w,\sigma,\ell,m}$ at individual ℓ.

Following the same way as the cross-correlation, we can define the ratio of RMS

amplitude $R_{\ell_w,\sigma}(\ell)$ between $T_{\ell,m}$ and $\tilde{T}_{\ell_w,\sigma,\ell,m}$ to be a function of ℓ as

$$R_{\ell_w,\sigma}(\ell) = \sqrt{\frac{\sum_{m=-\ell}^{\ell} \tilde{T}^2_{\ell_w,\sigma,\ell,m}}{\sum_{m=-\ell}^{\ell} T^2_{\ell,m}}}. \tag{9}$$

Fig. 5 shows $R_{\ell_w,\sigma}(\ell)$, the RMS ratio between the original and transformed fields, for $\ell_w = 2$ to 64. $R_{\ell_w,\sigma}(\ell)$ directly represents the transform from $T_{\ell,m}$ into $\tilde{T}_{\ell_w,\sigma,\ell,m}$ in the spectral domain and is an expression of a bandpass filter in spherical harmonics, which is equivalent to our wavelet-like transform. The plots in Fig. 5 can simply be approximated by a Gaussian function

$$R_{\ell_w,\sigma}(\ell) \approx R_\sigma \cdot \exp\left(-\left(\frac{4(\ell-\ell_w)}{\sigma\ell_w}\right)^2\right), \tag{10}$$

where $R_\sigma = 0.5823$ and is a constant which does not vary with ℓ_w. However, this can be considered as a zeroth-order approximation, and it is difficult to represent $R_{\ell_w,\sigma}(\ell)$ with a simple expression. The width of $R_{\ell_w,\sigma}(\ell)$ is roughly inversely proportional to σ, the width of the kernel. The shape of the plots in Fig. 5 would be different with a different kernel or mother wavelet.

Here $K_{\ell_w,\sigma}(\ell)$, the RMS power spectrum of the kernel (Eq. 5), can be calculated as

$$K_{\ell_w,\sigma}(\ell) = \sqrt{\sum_{m=-\ell}^{\ell} K^2_{\ell_w,\sigma,\ell,m}}, \tag{11}$$

where $K_{\ell_w,\sigma,\ell,m}$ is a set of coefficients taken from a spherical harmonic expansion of the kernel. We found that $K_{\ell_w,\sigma}(\ell)$ is very close to the ratio $R_{\ell_w,\sigma}(\ell)$ with an appropriate normalization;

$$R_{\ell_w,\sigma}(\ell) \approx \frac{K_{\ell_w,\sigma}(\ell)}{\sqrt{2\ell_w+1}} \tag{12}$$

The solid line in each panel Fig. 5 is drawn using the normalized $K_{\ell_w,\sigma}(\ell)$ (Eq. 12) for comparison with the plotted $R_{\ell_w,\sigma}(\ell)$ for each ℓ_w. We have confirmed numerically

that the relation in Eq. 12 holds for any values of ℓ_w and σ. However, as can be seen in Fig. 5, $R_{\ell_w,\sigma}(\ell)$ and $K_{\ell_w,\sigma}(\ell)$ are slightly different in the same manner for all the ℓ_w. To find an analytical relationship between $R_{\ell_w,\sigma}(\ell)$ and $K_{\ell_w,\sigma}(\ell)$ will require more work.

We note that $R_{\ell_w,\sigma}(\ell)$ represents a set of filters for mapping $T(\phi,\theta)$ into $\tilde{T}_{\ell_w,\sigma}(\phi,\theta)$. In addition, the shape of $R_{\ell_w,\sigma}(\ell)$ remains almost unchanged for $\ell_w \geq 8$. Therefore one can directly determine $\tilde{T}_{\ell_w,\sigma}(\phi,\theta)$ from $T(\phi,\theta)$ without having to calculate the transform by the arduous work in computing the convolution (Eq. 7) each time;

$$\tilde{T}_{\ell_w,\sigma}(\phi,\theta) = \sum_{\ell=0}^{\ell_{max}} \left(R_{\ell_w,\sigma}(\ell) \sum_{m=-\ell}^{\ell} T_{\ell,m} Y_{\ell,m}(\phi,\theta) \right) \tag{13}$$

However, one must be very careful with the numerical precision of $R_{\ell_w,\sigma}(\ell)$ of the lower-most ℓ for the cases with higher ℓ_w. This caution is necessitated by the fact that the geophysical data often contains very strong power at the lowest degrees of the spherical harmonic, which still has significant amplitude even after the filtering.

In this connection, Fig. 6 shows $\sqrt{\sum_{m=-\ell}^{\ell} \tilde{T}^2_{\ell_w,\sigma,\ell,m}}$, the RMS power of the transformed topography as a function of ℓ, for every transforms of $\ell_w = 2$ to 64 compared with that of original topography field. The sinusoidal envelope for all ℓ_w contains the same slope as the original topography, which means that our transform works out well in a wavelet-like manner.

5 Application to the Martian data from the MGS mission

We now apply our wavelet-like transform to the recently acquired Martian gravity data. We have used the GMM2B model (Lemoine et al., 2001) of the Martian gravity field, consisting of spherical harmonics coefficients up to degree and order 80. The Martian topography is taken from the GTM090AA model (Smith et al., 2000) going

up to degree 90. The topography data used here is based on a Martian radius relative to the Areoid based on the GMM2B model. In the further analyses, hydrostatic components of the gravity potential are eliminated from the GMM2B model with the method found in Goldreich and Toomre (1969). These gravity and topography data are presented in Fig. 7a and 7b respectively with the geographical names indicated by the arrows.

We carried out the wavelet-like transform defined by Eq. 7 to the Martian gravity and topography fields. The transformed fields for $\ell_w = 8$ (2662 km), 16 (1331 km), 32 (665 km), and 64 (333 km in wavelength), are shown in Fig. 7c and 7d, respectively, for the case that $\sigma = 2$. Of particular interest is the prominent signature of the Tharsis region at all of the scales examined, when we compare Figs. 7c and 7d with Figs. 7a and 7b, which show the original gravity and topography. One can also discern the regions Valles Marineris and Elysium up to $\ell_w = 64$. However, artificial oscillations with small amplitude has already been observed in the original gravity map, which also appeared in the wavelet transformed gravity fields for $\ell_w = 64$.

We have also shown the case for $\sigma = 4$ and $\sigma = 8$ in Fig. 8c and 8d and Fig. 9c and 9d, respectively. It is clear from a comparison of these two figures that the wiggles adjacent to the strong signals develop more with a larger σ due to a wider window of the kernel in the transform function.

6 Admittance and spatial correlation

The definition of admittance as used here is a linear transfer function, which represents a ratio of the amplitudes between gravity anomaly and topography for a selected wavelength component (e.g. McNutt and Parker, 1978). Here we define the spatially localized admittance as a slope calculated by least squares fit of plots for discretized

distribution of $\tilde{G}_{\ell_w,\sigma}(\phi,\theta)$ versus $\tilde{T}_{\ell_w,\sigma}(\phi,\theta)$. The discretized distribution of the two fields are confined in the same Gaussian window in the kernel centered at a point of spatial localization;

$$W_{\ell_w,\sigma}(\xi) = \exp\left(-\left(\frac{\ell_w \xi}{2\sigma}\right)^2\right) , \tag{14}$$

where ξ is the angular distance to the center. This window also acts as a weighting function in the least squares fitting for the slope. Therefore the estimate of the slope comes down to a simple least squares problem with the weighted data. Then we obtain the spatially localized admittance $Z_{\ell_w,\sigma}$ at a point (ϕ_0,θ_0) as a 2D map;

$$Z_{\ell_w,\sigma}(\phi_0,\theta_0) = \frac{\int_\Omega W_{\ell_w,\sigma}(\xi)\tilde{T}(\phi,\theta)\tilde{G}(\phi,\theta)d\Omega}{\int_\Omega W_{\ell_w,\sigma}(\xi)\tilde{T}^2(\phi,\theta)d\Omega} . \tag{15}$$

The spatial correlation between $\tilde{G}_{\ell_w,\sigma}(\phi,\theta)$ and $\tilde{T}_{\ell_w,\sigma}(\phi,\theta)$ is also an important quantity for the interpretation of the admittance, because the Airy's compensation requires that two fields are highly coherent for shorter wavelengths. The perfect isostasy for longer wavelength yields no gravity signal and results in poor coherence with topography. The nature of the coherence function also yields important information about the mechanical state of the lithosphere as well as the admittance function (e.g., Forsyth, 1985; Simons et al., 2000). Here, we define the spatially localized correlation $C_{\ell_w,\sigma}$ between the transformed fields $\tilde{G}_{\ell_w,\sigma}(\phi,\theta)$ and $\tilde{T}_{\ell_w,\sigma}(\phi,\theta)$ around a point (ϕ_0,θ_0) in the spatial domain with the weighting function of $W_{\ell_w,\sigma}(\xi)$ in the same way as in Eq. (15);

$$C_{\ell_w,\sigma}(\phi_0,\theta_0) = \frac{\int_\Omega W_{\ell_w,\sigma}(\xi)\tilde{T}(\phi,\theta)\tilde{G}(\phi,\theta)d\Omega}{\sqrt{\int_\Omega W_{\ell_w,\sigma}(\xi)\tilde{T}^2(\phi,\theta)d\Omega \int_\Omega W_{\ell_w,\sigma}(\xi)\tilde{G}^2(\phi,\theta)d\Omega}} . \tag{16}$$

Thus the calculated $Z_{\ell_w,\sigma}(\phi,\theta)$ and $C_{\ell_w,\sigma}(\phi,\theta)$ based on the GMM2B and GTM090AA models in the case of $\sigma = 2$ are shown respectively in Fig. 7e and 7f, for $\ell_w = 8$, 16, 32, and 64.

A poorly correlated region at shorter wavelengths usually indicates a breakdown of the simple assumption of the Airy model, which makes it difficult to infer the variations of the plate rigidity and the crustal thickness from the admittance value. In addition, the gravity data itself includes significant error for shorter wavelength components. Lemoine et al. (2001) reports that higher degrees of gravity data have been constructed with the help of Kaula's law (Kaula 1968), rather than observations alone. Furthermore, the correlation usually becomes higher with increasing degree, because only the topographic loading at the surface with crust of an uniform density will be dominant in such a short wavelength. Therefore, the region with poor correlation for $\ell_w = 64$ mainly comes from the artificial noise in the gravity data. For these reasons, we believe that the region with poor correlation should be excluded for further interpretation of the admittance value, especially for higher degrees. Fig. 7g is the admittance map as in Fig. 7e, but the region with poor correlation are masked in a graphical sense by superimposing it with a black shade. From now on, we will discuss the admittance map based on Fig. 7g.

The difference among the three values of σ becomes much clearer in the local admittance and spatial correlation function rather than the transformed fields. The larger σ (Fig. 8g and Fig. 9g) apparently averages the lateral information of the admittance and correlation and stabilizes their patterns. We will consider the optimal choice of the value of σ in the discussion section.

7 Interpretation

For the case in $\sigma = 2$ in Fig. 7, regions of unstable admittance value (red-blue oscillation) are observed, especially in the northern hemisphere. In these regions the artificial noise of gravity frequently changes in sign, while the topography is small but stable due to the nature of the dichotomy of the Martian topography (Hartmann,

1993). This results in an unstable behavior with a large amplitude of admittance for $\ell_w = 64$. This is due to the fact that the denominator of the admittance ratio is the gravity, while the numerator represents the topography. Correlation must have the same sign as the admittance by definition. However, the correlation is generally small in these regions with artificial noise. By excluding these noisy areas, we can bring about a clearer picture by juxtaposing the admittance function together with the correlation function.

The lithospheric strength can be estimated by the admittance function dropping sharply at a threshold wavelength (Ricard et al., 1984 and Fig.1 of McKenzie et al., 2002). From Fig. 7g, we can easily discern the threshold in the Tharsis region to lie between $\ell_w = 16$ and 32, which can be interpreted as a relatively rigid lithosphere. On the other hand, in the Valles Marineris region, the admittance function remains still small even for short wavelengths, which implies a weak lithosphere or a less dense crustal material in this region. These results are basically compatible with the findings of McKenzie et al. (2002), who performed regional admittance study using a highly reliable raw orbital data.

The admittance in the Tharsis region does not become zero even for $\ell_w = 8$, which indicates the existence of the dynamical support by mantle convection. This may be caused by the east to west degree one structure of the convective system in the underlying Martian mantle (Matyska et al., 1998; Zhong and Zuber, 2001). On the other hand, no significant admittance changes are observed across the boundary of the north-south dichotomy. This topographic dichotomy apparently originates in a different crustal thickness (e.g., McGill and Dimitriou, 1990; Zuber et al., 2000), which yields less of a contribution to the admittance function. Therefore, we do not expect any coupling from the variations in the Martian crustal thickness to the underlying mantle circulation at long wavelengths and the effective thickness of the

elastic lithosphere at shorter wavelengths. The presence of this decoupling of the crust from the underlying lithosphere and mantle circulation may provide valuable new insight into the formation of the Northern Martian hemisphere, which now becomes an exciting, hot, new issue raised by the recent discovery of numerous buried craters in the Northern Hemisphere (Frey et al., 2002; Solomon, 2002).

We can observe negative admittance for $\ell_w = 16$ in Utopia, Isidis, and Argyre region in Fig. 7 for $\ell_w = 16$. These regions correspond to large craters with gravity high and topographic low. However Hellas, the largest crater in Mars, has no strong signal in the admittance. A possible explanation for this is due to a different type of infilled material from those in other craters. Since the crater landform is a quite localized feature, characteristic of signals due to a negative admittance now disappear in the case of $\sigma = 8$ (Fig. 9) because of its wide spatial window in the kernel.

8 Concluding Remarks and Discussion

In this paper we have laid out a relatively simple algorithm for constructing wavelet-like transforms on a spherical surface, which will have wide applications in geophysics. Our method calls for making a geometrical correction to a Gabor-type transform kernel, which has been rotated over a Cartesian plane. The advantages of using a Gabor-type transform lies in its localization capability with changing σ, as compared to the Gaussian-type wavelets. Besides the Gabor-type transform, any types of isotropic wavelets on 2D Cartesian geometry, can be applied to the spherical surface by using the geometrical correction defined in this study. We note that the choice of mother wavelets makes little difference in the analysis results. Exerting a careful balance of the spatial and wavelength localization for the same type of wavelet will influence greatly the transformed results. Its importance cannot be more strongly emphasized.

We emphasize that the strength of our method lies more in its analytical simplicity rather than on its raw computational speed, which may be achieved faster with discrete wavelet methods (Freeden and Windheuser, 1998; Li, 1999). Fast discrete spherical transform method (Lesur and Gubbins, 1999), the spherical multigrid method (Stuhne and Peltier, 1999), or the localized trigonometric functions (Mohlenkamp, 1999) can also be helpful in this endeavor. The simplicity of our method also allows this algorithm to be parallelized easily, as one can divide up the segments of the line integral and compute on a cluster of computers the summation of the contributions in the convolution integral.

We have demonstrated that this wavelet-like transform can be described as a Gaussian bandpass filter, expanded in spherical harmonics, similar to what we had done before with Cartesian 2D wavelets (Yuen et al., 2002). This filtering property of the spherical filter has also been demonstrated numerically for various length scales. From our construction of this wavelet-like transform, we have distilled a useful prescription for computing this filter, which allows one to calculate this wavelet-like transform with multiresolution capabilities in terms of spherical harmonics, as in the approach of bandpass filter by Simons et al. (1997).

We need to go to the admittance map for a better understanding of the lateral variation of the Martian lithosphere, because of the predictive power of the admittance function (Ricard et al., 1984). In Fig. 7e and 7f, we show the 2D maps of the localized admittance and correlation. Simons et al. (1997) have conducted a localized admittance study on the Venusian surface by using a windowed function constructed in terms of the spherical harmonics and its triple products. This approach is computationally demanding and has been applied to Martian surface by McGovern et al. (2000). The major advantage of our wavelet approach is that all the computation procedures are carried out in the spatial domain, using a grid data structure. This

allows us to handle the analysis of a finite region of interest with a high-resolution grid of data on the Earth (e.g., McKenzie and Fairhead, 1997). The spatial domain treatment is also useful for Lunar analysis, where constructing spherical harmonic coefficients is difficult due to the lack of data over a large region (Wieczorek and Phillips, 1998). Another advantage is that we can estimate the spatial reliability of the admittance map by introducing the localized correlation quantity. From Fig. 7g we can discern that there are regions of reliability even at the shortest scales. In the classical fully spectral approach, global correlation over such short scales would be of too low quality to be useful.

The spatial window size is σ/ℓ_w and is proportional to the wavelength, which is a typical character in the wavelet analyses. The σ, which controls the localization balance, is the most effective quantity in the admittance analysis. We have shown, for a fixed value of σ, a series involving the various scales (ℓ_w from 8 to 64) of the transformed field, the admittance function and the correlation fields. Some artificial oscillations are observed at $\ell_w = 64$ using $\sigma = 2$ in Fig. 7. It is obvious that the window size is too small compared to the reliable spatial resolution of the gravity data. In this case we should employ wider window, such as $\sigma = 4$ or 8. On the contrary, for longer wavelength at $\ell_w = 16$, the choice of $\sigma = 2$ is reasonable. As end members in this scheme of optimizing the size of the window, one can impose the size of the window independent of the wavelength rather than fix the value of σ. When we consider the physical interpretation of the admittance function in terms of the mechanical state of the lithosphere, which represents a fully spatial property, we can see that fixing the window size is the appropriate action to take. Simons et al. (1997) had optimized analytically the fixed window size in the spatial domain, based on the Nyquist criterion of the wavelength of the data being resolved. However, in the presence of data with significant noise, the optimization of the window size would

be fraught with severe technical difficulties.

Even in the face of possible error contamination of the spherical harmonic gravity data employed here and the uncertainties in the choice of the window size, we maintain that mapping out the local admittance function over the sphere can yield significant valuable insights into the nature of the lateral variations of the Martian lithosphere. The physical interpretation of the admittance function in terms of a continuous field description of the mechanical state of the lithosphere, and not at discrete sites, represents the next challenging issue. Even a partial resolution of this problem will go a long way in helping us to understand the underlying dynamical cause of the Tharsis bulge (Thomas and Allemand, 1993).

Wavelets combined with higher resolution data from specialized missions, such as the Martian Orbiter Laser Altimeter (MOLA), may help to shed light on the dynamics of the fine structures of the Martian lithosphere, as recent modelling efforts of faults by Barnett and Nimmo (2002) have demonstrated.

Acknowledgment. We thank discussions with Stephen Y. Bergeron, Ludek Vecsey, and T.K.B. Yanagawa. Reviewer's suggestions have greatly improved the quality of this paper. This research was supported by geophysics program of the National Science Foundation and a travel grant to M. Kido by the Univ. Minnesota Supercomputing Institute.

References

Antoine, J.-P., Jacques, L., and Vandergheynst, P., 2002. Wavelets on the sphere: Implementation and approximation. Applied and Computational Harmonic Analysis, in press.

Arkani-Hamed, J., 2000. Strength of Martian lithosphere beneath large volcanoes. J. Geophys. Res., 105: 26713–26732.

Barnett, D.M. and Nimmo, F., 2002. Strength of faults on Mars from MOLA topography. Icarus, 157, No.1: 24–42.

Bergeron, S.Y., Vincent, A.P., Yuen, D.A., Tranchant, B.J.S., and Tchong, C., 1999. Viewing seismic velocity anomalies with 3-D Continuous Gaussian wavelets. Geophys. Res. Lett., 26: 2311–2314.

Bergeron, S.Y., Yuen, D.A., and Vincent, A.P., 2000. Capabilities of 3-D wavelet transforms to detect plume-like structures from seismic tomography. Geophys. Res. Lett., 27: 3433–3436.

Chiao, L.-Y., and Kuo, B.Y., 2001. Multiscale seismic tomography. Geophys. J. Int., 145: 517–527.

Daugman, J.G., 1985. Uncertainty relation for resolution in space, spatial frequency, and orientation optimized by two-dimensional visual cortical filters. J. Optical Soc. America A, 2: 1160–1169.

Folland, G.B., 1989. Harmonic Analysis in Phase Space. Princeton Univ. Press: pp. 288.

Forsyth, D.W., 1985. Subsurface loading and estimates of the flexural rigidity of continental lithosphere. J. Geophys. Res., 90: 12623–12632.

Freeden, W., and Schreiner, M., 1995. Non-orthogonal expansions on the sphere. Math. Meth. Appl. Sci., 18: 83–120.

Freeden, W., and Windheuser, U., 1996. Spherical wavelet transform and its discretization. Adv. Comput. Math., 5: 51–94.

Freeden, W., and Windheuser, U., 1998. Combined spherical harmonic and wavelet expansion — A future concept in Earth's gravitational determination. Appl. Comput. Harmonic Analy., 4: 1–37.

Frey, H.V., Roark, J.H., Shockey, K.M., Frey, E.L., and Sakimoto, S.E.H., 2002. Ancient lowlands on Mars. Geophys. Res. Lett., 29 No.10: 10.1029/2001GL013832.

Gabor, D., 1946. Theory of Communication. J. IEEE (London), 93 III No. 26: 429–457.

Gibert, D., Hohlschneider, M., and Le Mouel, J.-L., 1998. Wavelet analysis of the Chandler Wobble. J. Geophys. Res., 103: 27069–27089.

Goldreich, P., and Toomre, A., 1969. Some remarks on polar wandering, J. Geophys. Res., 74: 2555–2567.

Guyodo, Y., Gaillot, P., and Channell, J.E.T., 2000. Wavelet analysis of relative geomagnetic paleointensity at ODP Site 983. Earth Planet. Sci. Lett., 184: 109–123.

Hartmann, W. K., 1993. Moons and Planets, Wordsworth, Belmont, CA, 510 pp.

Kaula, W. M., 1968. An Introduction to Planetary Physics, The Terrestrial Planets. John Wiley, New York.

Kumar, P., and Foufoula-Georgiou, E., 1997. Wavelet analysis for geophysical applications. Rev. Geophys., 35: 385–412.

Lemoine, F. G., Smith, D.E., Rowlands, D.D., Zuber, M.T., Neumann, G.A., Chinn, D.S., and Pavlis, D.E., 2001. An improved solution of the gravity field of Mars (GMM-2B) from Mars Global Surveyor. J. Geophys. Res., 106: 23359–23376.

Lesur, V., and Gubbins, D., 1999. Evaluation of fast spherical transforms for geophysical applications. Geophys. J. Int., 139: 547–555.

Li, T.-H., 1999. Multiscale representation and analysis of spherical data by spherical wavelets. S.I.A.M., J. Sci. Comput., 21: 924–953.

Malamud, B.D., and Turcotte, D.L., 2001. Wavelet analyses of Mars polar topography. J. Geophys. Res., 106: 17498–17504.

Mallat, S., 1998. A Wavelet Tour of Signal Processing, Academic Press, Boston.

Matyska, C., Yuen, D.A., Breuer, D., and Spohn, T., 1998. Symmetries of volcanic distributions on Mars and Earth and their mantle plume dynamics. J. Geophys. Res., 103: 28587–28597.

McGill, G.E., and Dimitriou, A.M., 1990. Origin of the Martian global dichotomy by crustal thinning in the late Noachian or early Hesperian. J. Geophys. Res., 95: 12595–12605.

McGovern, P.J., Solomon, S.C., Smith, D.E., Zuber, M.T., Neumann, G.A., and Head, J.W., 2000. Localized gravity/topography admittance on Mars. Lunar Planet. Sci., 31: abstract 1792.pdf.

McKenzie, D., and Fairhead, D., 1997. Estimates of the effective elastic thickness of the continental lithosphere from Bouguer and free air gravity anomalies. J. Geophys. Res., 102: 27523–27552.

McKenzie, D., Barnett, D.N., and Yuan, D.-N., 2002. The relationship between Martian gravity and topography. Earth Planet. Sci. Lett., 195: 1–16.

McNutt, M.K., and Parker,R.L., 1978. Isostasy in Australia and the evolution of the compensation mechanism. Science, 199: 773–775.

Mohlenkamp, M.J., 1999. A fast transform for spherical harmonics. J. Fourier Anal. Appl., 5: 159-184.

Moreau, F., Gibert, D., Hohlschneider, M., and Saraaco, G., 1999. Identification of sources of potential fields with the continuous wavelet transform: Basic theory. J. Geophys. Res., 104: 5003–5013.

Narcowich, F.J., and Ward, J.D., 1996. Nonstationary wavelets on the m-sphere for scattered data. Appl. Comput. Harmonic Analy., 3: 324–336.

Piromallo, C., Vincent, A.P., Yuen, D.A., and Morelli, A., 2001. Dynamics of the transition zone under Europe inferred from wavelet cross-spectra of seismic tomography. Phys. Earth Planet. Inter., 125: 125-139.

Ricard, Y., Fleitout, L., and Froidevaux, C., 1984. Geoid heights and lithospheric stresses for a dynamic Earth. Annal. Geophysicae, 2: 267–286.

Simons, F.J., Zuber, M.T., and Korenaga, J., 2000. Isostatic response of the Australian lithosphere: Estimation of effective elastic thickness and anisotropy using multitaper spectral analysis. J. Geophys. Res., 105: 19163–19184.

Simons, M., Solomon, S.C., and Hager, B.H., 1997. Localization of gravity and topography: constraints on the tectonics and mantle dynamics of Venus. Geophys. J. Int., 131: 24–44.

Smith, D.E., Sjogren, W.L., Tyler, G.L., Balmino, G., Lemoine, F.G., and Konopliv, A.S., 1999a. The gravity field of Mars: Results from Mars Global Surveyor. Science, 286: 94–97.

Smith, D.E., Neumann, G., Ford, P, Arvidson, R.E., Guinness, E.A., and Lavney, S.S., 1999b. Mars Global Surveyor Laser Altimeter Initial Experiment Gridded Data Record. NASA Planetary Data System, MGS-M-MOLA-5-IEGDR-L3-V1.0.

Smith, D.E., Zuber, M.T., Solomon, S.C., Phillips, R.J., Head, J.W., Garvin, J.B., Banerdt, W.B., Muhleman, D.O., Pettengill, G.H., Neumann, G.A., Lemoine, F.G., Abshire, J.B., Aharonson, O., Brown, C.D., Hauck, S.A., Ivanov, A.B., McGovern, P.J., Zwally, H.J., and Duxbury, T.C., 1999c. The global topography of Mars and implications for surface evolution. Science, 284: 1495–1503.

Smith, D., Neumann, G., and Simpson, R., 2000. Mars Global Surveyor Laser Altimeter Initial Experiment Gridded Data Record: NASA Planetary Data System, MGS-M-MOLA-5-IEGDR-L3-V1.0.

Smith, D.E., Zuber, M.T., Frey, H.V., Garvin, J.B., Head, J.W., Muhleman, D.O., Pettengill, G.H., Phillips, R.J., Solomon, S.C., Zwally, H.J., Banerdt, W.B., Duxbury, T.C., Golombek, M.P., Lemoine, F.G., Neumann, G.A., Rowlands, D.D., Aharonson, O., Ford, P.G., Ivanov, A.B., McGovern, P.J., Abshire, J.B., Afzal, R.S., and Sun, X., 2001. Mars Orbiter Laser Altimeter (MOLA): Experiment summary after the first year of global mapping of Mars. J. Geophys. Res., 106: 23,689–23,722.

Solomon, S.C., 2002. An older face for Mars. Nature, 418: 27–28.

Stacey, F.D., 1992. Physics of the Earth, Third edition. Brookfield Press, Brisbane, 427 p.

Stuhne, G.R., and Peltier, W.R., 1999. New icosahedral grid-point discretizations of the shallow water equations on the sphere. J. Comput. Phys., 148: 23–58.

Thomas, F.G., and Allemand, P., 1993. Quantitative analysis of extensional tectonics of Tharsis bulge, Mars: Geodynamic implications. J. Geophys. Res., 98: 13,097–13,108.

Turcotte, D.L., Shcherbakov, R., Malamud, B.D., and Kucinskas, A.B., 2002. In the Martian crust also the Martian elastic lithosphere? J. Geophys. Res., in press.

Vecsey, L., and Matyska, C., 2001. Wavelet spectra and chaos in thermal convection modelling. Geophys. Res. Lett., 28: 395–398.

Wieczorek, M.A., and Phillips, R.J., 1998. Potential anomalies on a sphere: Applications to the thickness of the lunar crust. J. Geophys. Res., 103: 1715–1724.

Yuan, D.-N., Sjogren, W.L., Konopliv, A.S., and Kucinskas, A.B., 2001. Gravity field of Mars: A 75th degree and order model. J. Geophys. Res., 106: 23377–23401.

Yuen, D.A., Vincent, A.P., Kido, M., and Vecsey, L., 2002. Geophysical applications of multidimensional filtering using wavelets. Pure Appl. Geophys., 159: 2285–2309.

Zhong, S., and Zuber, M.T., 2001. Degree-1 mantle convection and the crustal dichotomy on Mars. Earth Planet. Sci. Lett., 189: 75–84.

Zuber, M.T., Smith, D.E., Solomon, S.C., Muhleman, D.O., Head, J.W., Garvin, J.B., Abshire, J.B., and Bufton, J.L., 1992. The Mars Observer Laser Altimeter investigation. J. Geophys. Res., 97: 7781–7798.

Zuber, M.T., Solomon, S.C., Phillips, R.J., Smith, D.E., Tyler, G.L., Aharonson, O., Balmino, G., Banerdt, W.B., Head, J.W., McGovern, C.L., Neumann, G.A., Rowlands, D.D., and Zhong, S., 2000. Internal structure and early thermal evolution of Mars from Mars Global Surveyor topography and gravity. Science, 287: 1788–1793.

Zuber, M.T., 2001. The crust and mantle of Mars. Nature, 412: 220–227.

Figure captions

Fig. 1. Morphology of the mother wavelet or kernel (left column), window (middle column), and basis function (right column) in a Cartesian geometry. Figures in the top row show the composition of 2D anisotropic Gabor wavelet (Daugman, 1985) and at the bottom row show that of an isotropic wavelet defined in this study, which is generated by averaging the above anisotropic wavelet along the azimuthal direction.

Fig. 2. (a) Kernel of the wavelet-like transform used in this study plotted as a function of angular distance ξ in Eq. 5 ($\ell_w = 8$, $\sigma = 2$). Dotted curve is the Bessel function $J_0(\ell_w \xi)$, and short dashed line is with the spherical correction $J_0(\ell_w \xi)\xi / \sin \xi$. The zero-mean adjustment (denoted by DC) is relatively small (long dashed line). Solid line is a final shape of Eq. 5 with the window except for the normalization term. (b) Plots of Eq. 5 (without the normalization) for each ℓ_w. To compare them at the same scale, the horizontal axis is scaled as $\xi \ell_w / 4$. We show the plots for $\ell_w = 2$, 3, 4, 5, 8, 16. The singular behavior is due to the spherical correction at the antipodes, discussed in the text. We note that the difference in the function near $\xi \ell_w / 4 = 60^\circ$ violates the wavelet requirement of similarity of the figures in each ℓ_w. However, the difference can not be distinguished for $\ell_w \geq 8$.

Fig. 3. Illustration of the process for constructing a wavelet-like transform (Eq. 7) of the topographic field on the sphere. (a) is transformed topography at corresponding degree $\ell_w = 8$ and $\sigma = 2$. The transformed topography at a point (ϕ_0, θ_0) indicated by a star in (a) consists of convolution of the original field (b) and the kernel (Eq. 5) centered at the corresponding point (c) on the sphere. The topography data is taken from the GTM090AA model (Smith et al., 2000) going up to spherical harmonics of degree 90.

Fig. 4. Cross-correlation $C_{\ell_w,\sigma}(\ell)$ for individual degree component between the original topography $T_{\ell,m}$ and spherical harmonics expansion of the transformed topography $\tilde{T}_{\ell_w,\sigma,\ell,m}$ defined by Eq. 8. Corresponding degrees ℓ_w are 2 to 64, as indicated in each panel. The values of $C_{\ell_w,\sigma}(\ell)$ are nearly unity for any of ℓ_w and ℓ. In each panel the degrees ℓ, ranging only from 2 to $2\ell_w$, are shown, since there is almost no power in the components for ℓ larger than $2\ell_w$.

Fig. 5. Plot of the diamonds are the RMS power spectrum ratio $R_{\ell_w,\sigma}(\ell)$ between spherical harmonics expansion of the transformed topography $\tilde{T}_{\ell_w,\sigma,\ell,m}$ and the original topography $T_{\ell,m}$ defined by Eq. 9 for $\ell_w = 2$ to 64. Curves of solid lines are obtained by a different way (Eq. 12). In each panel, degree ℓ ranging only from 2 to $2\ell_w$ are shown, since there is almost no power in components for ℓ larger than $2\ell_w$.

Fig. 6. The RMS power spectra of the transformed topography as a function of ℓ for all of the cases of $\ell_w = 2$ to 64, indicated within the panel. RMS power spectrum of the original topography (Smith et al., 2000) is also shown for comparison.

Fig. 7. Original (a) gravity and (b) topography fields for Martian surface. Wavelet transformed (c) gravity and (d) topography, and spatially localized (e) admittance and (f) correlation for $\ell_w = 8$, 16, 32, and 64 in the case of $\sigma = 2$ are also shown. Corresponding wavelengths for ℓ_w are 2662, 1331, 665, and 333 km, respectively. In (g), the admittance has been masked by black shade where the absolute value of the correlation is extremely small.

Fig. 8. The same as Fig. 7 but in the case of $\sigma = 4$.

Fig. 9. The same as Fig. 7 but in the case of $\sigma = 8$.

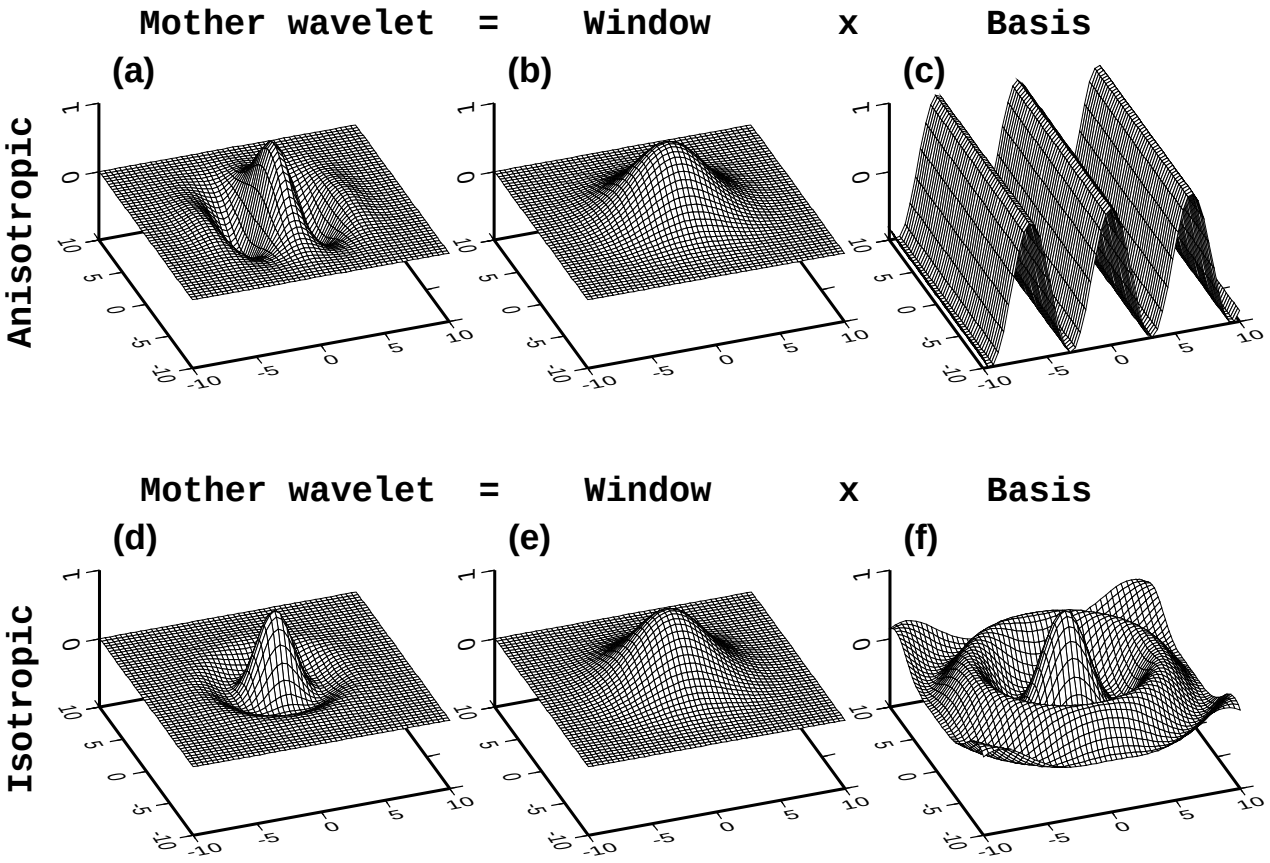
Mother wavelet = Window x Basis
(a)
(b)
(c)
Anisotropic
Mother wavelet = Window x Basis
(d)
(e)
(f)
Isotropic

Fig. 1

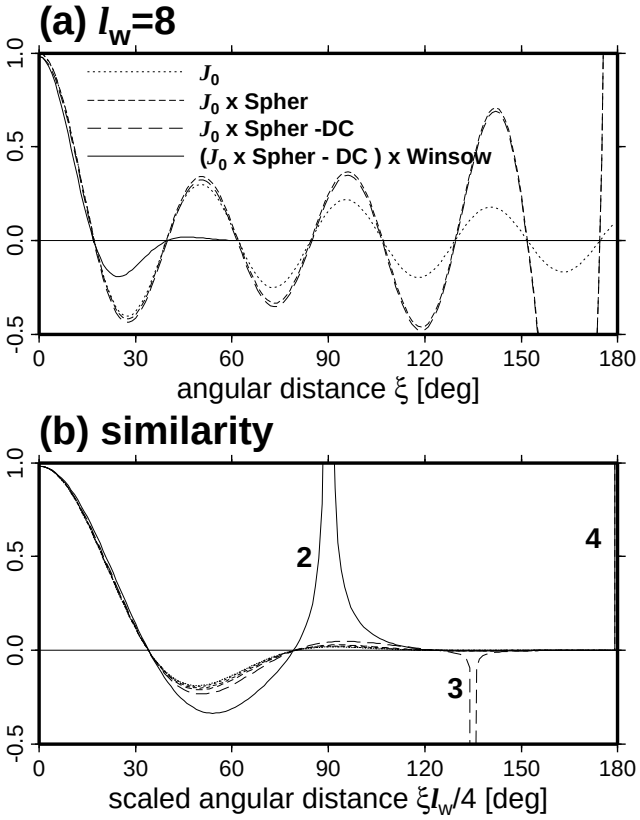
(a) l_w=8
J_0
J_0 x Spher
J_0 x Spher -DC
(J_0 x Spher - DC) x Winsow
1.0
0.5
0.0
-0.5
0
30
60
90
120
150
180
angular distance ξ [deg]
(b) similarity
2
3
4
scaled angular distance ξl_w/4 [deg]

Fig. 2

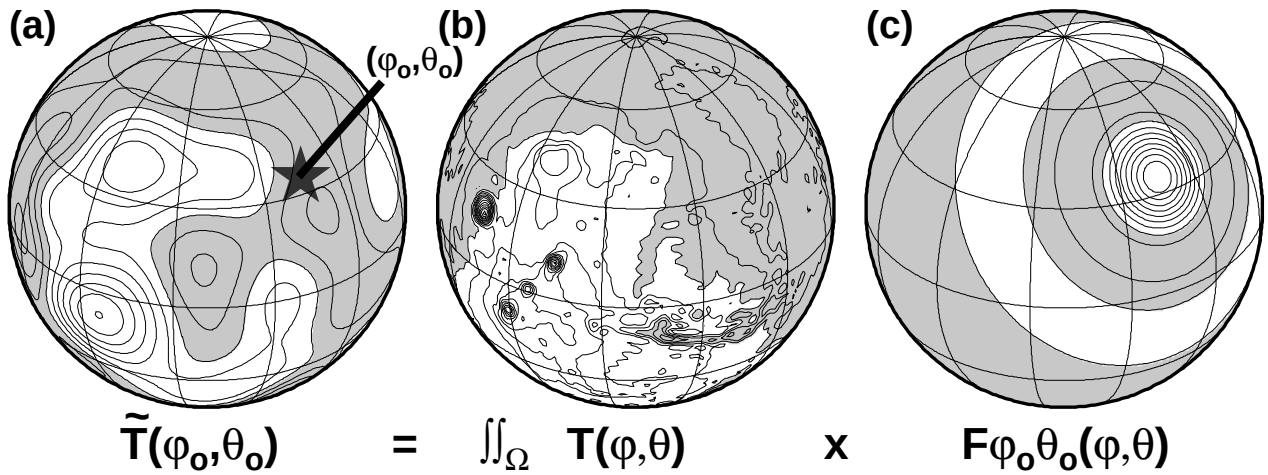
(a)
(b)
(c)
(φ_o,θ_o)
$\tilde{T}(\varphi_o,\theta_o)$ = $\iint_\Omega$ $T(\varphi,\theta)$ x $F\varphi_o\theta_o(\varphi,\theta)$

Fig. 3

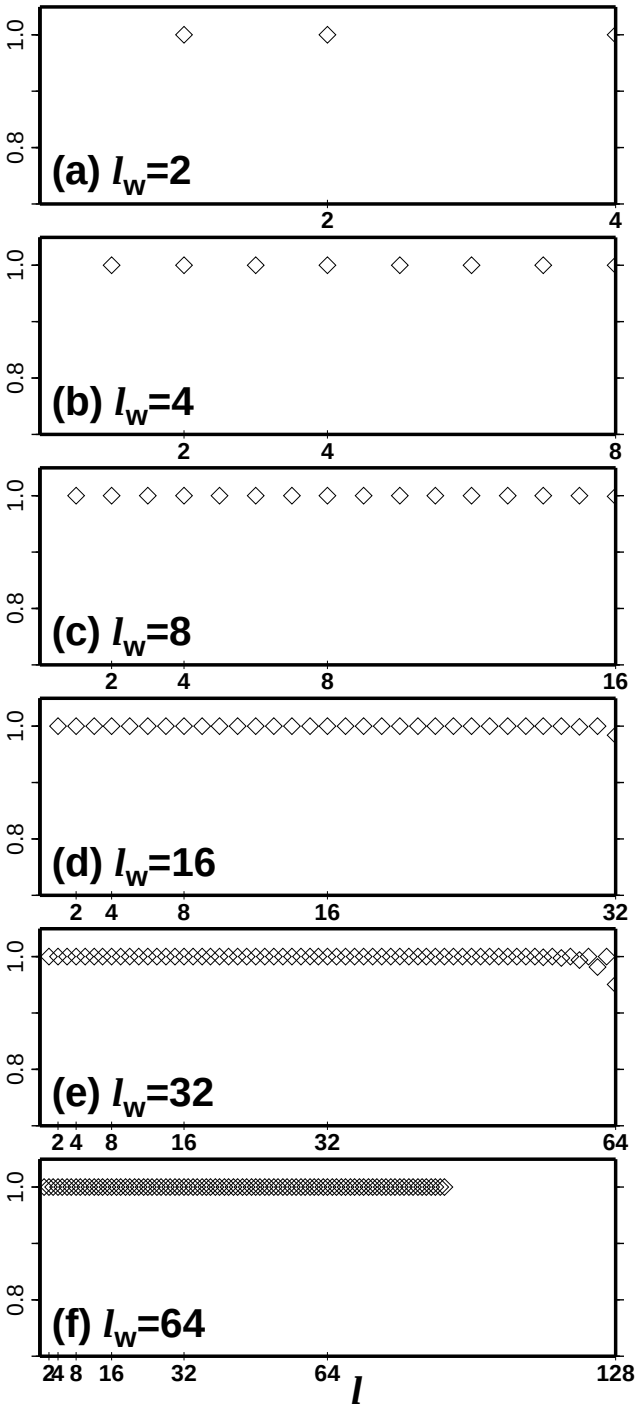
1.0
0.8
(a) l_w=2
2
4
(b) l_w=4
2
4
8
(c) l_w=8
2
4
8
16
(d) l_w=16
2
4
8
16
32
(e) l_w=32
2
4
8
16
32
64
(f) l_w=64
2
4
8
16
32
64
128
l

Fig. 4

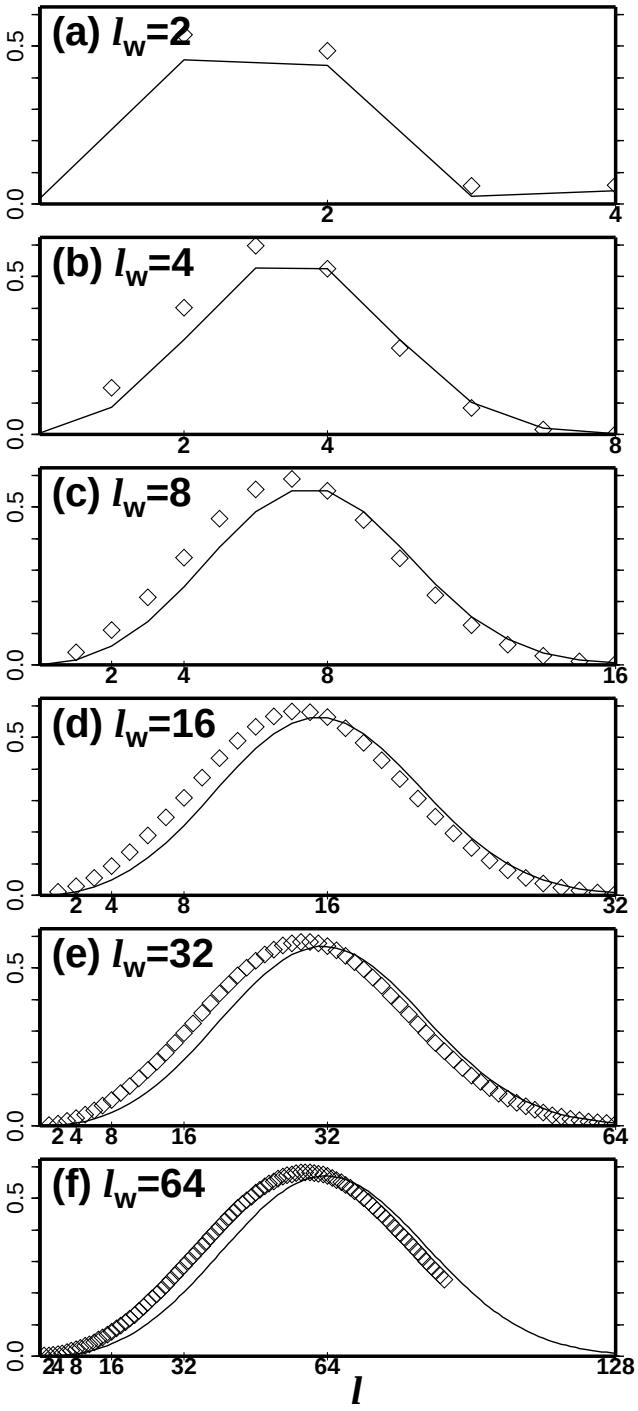

Fig. 5

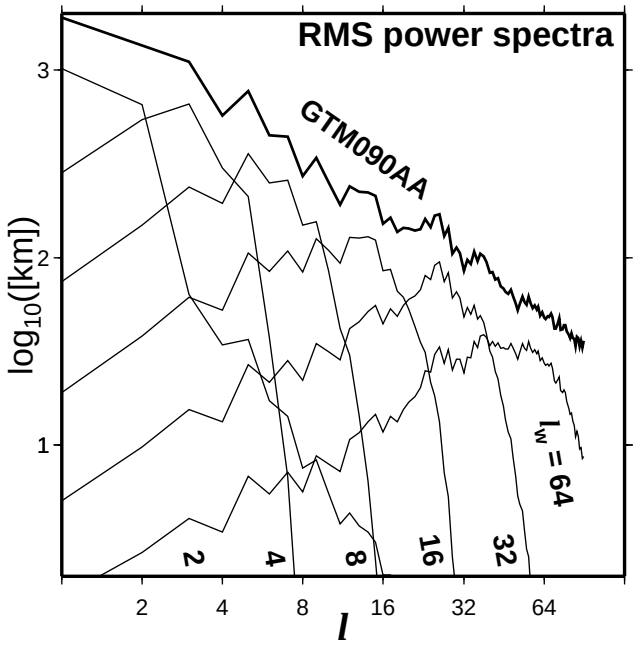
RMS power spectra
GTM090AA
l_w = 64
2
4
8
16
32
3
2
1
$\log_{10}([km])$
2
4
8
16
32
64
l

Fig. 6

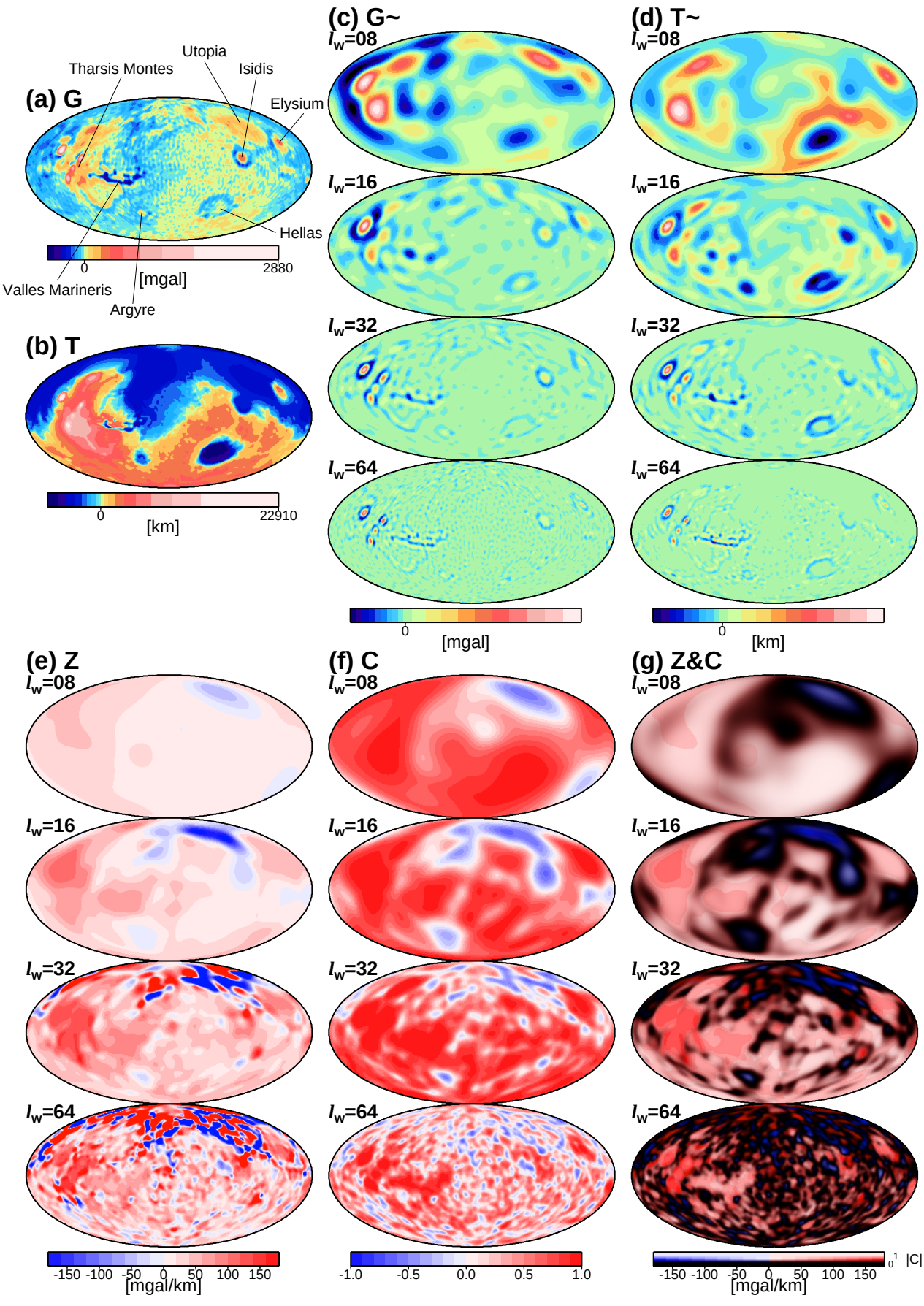
(a) G
Tharsis Montes
Utopia
Isidis
Elysium
Hellas
Valles Marineris
Argyre
0
2880
[mgal]
(b) T
0
22910
[km]
(c) G~
(d) T~
lw=08
lw=16
lw=32
lw=64
0
[mgal]
0
[km]
(e) Z
(f) C
(g) Z&C
-150 -100 -50 0 50 100 150
[mgal/km]
-1.0 -0.5 0.0 0.5 1.0
0 1 |C|
-150 -100 -50 0 50 100 150
[mgal/km]

Fig. 7

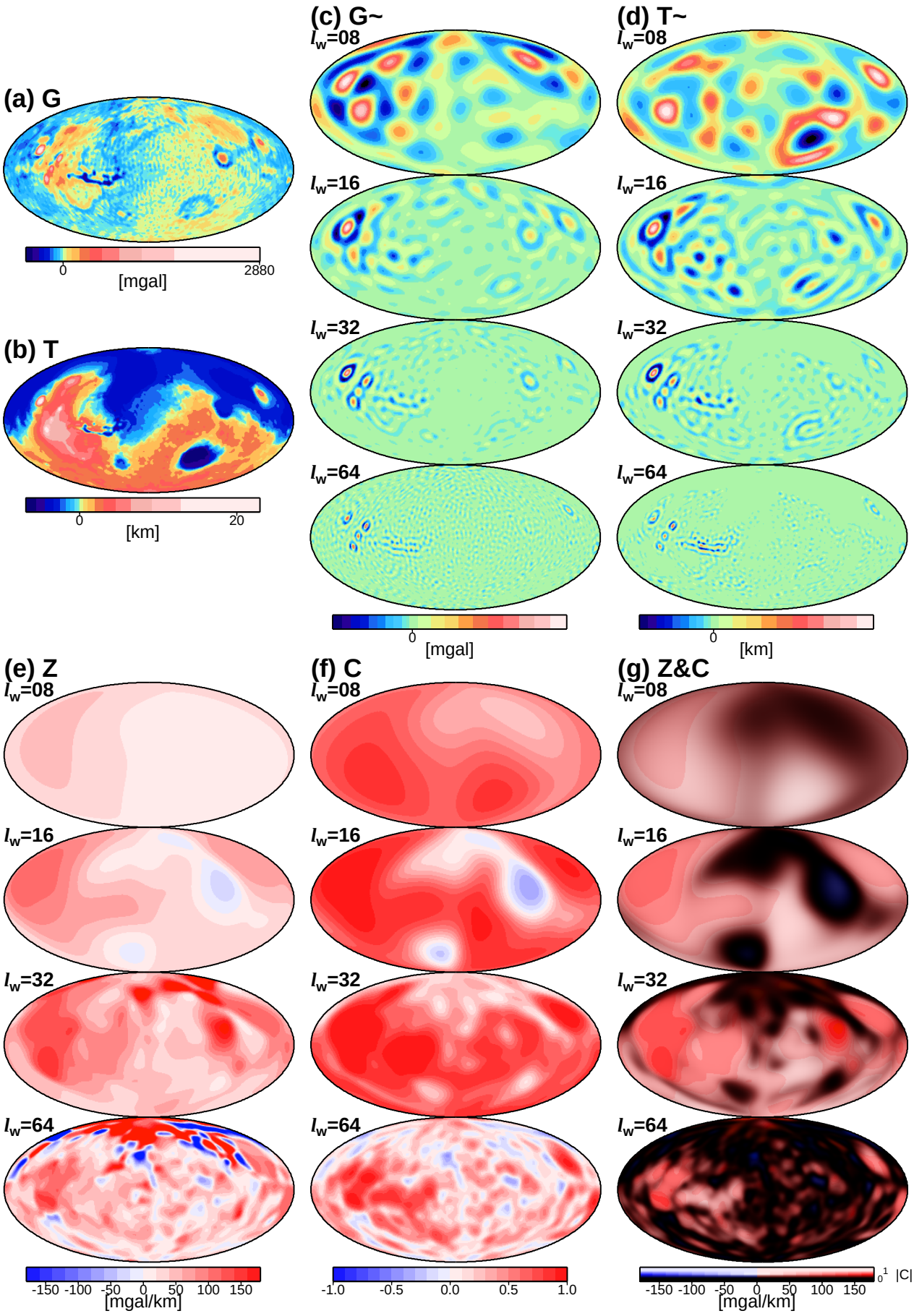
(a) G
0
2880
[mgal]
(b) T
0
20
[km]
(c) G~
l_w=08
l_w=16
l_w=32
l_w=64
0
[mgal]
(d) T~
l_w=08
l_w=16
l_w=32
l_w=64
0
[km]
(e) Z
l_w=08
l_w=16
l_w=32
l_w=64
-150 -100 -50 0 50 100 150
[mgal/km]
(f) C
l_w=08
l_w=16
l_w=32
l_w=64
-1.0 -0.5 0.0 0.5 1.0
(g) Z&C
l_w=08
l_w=16
l_w=32
l_w=64
0 1 |C|
-150 -100 -50 0 50 100 150
[mgal/km]

Fig. 8

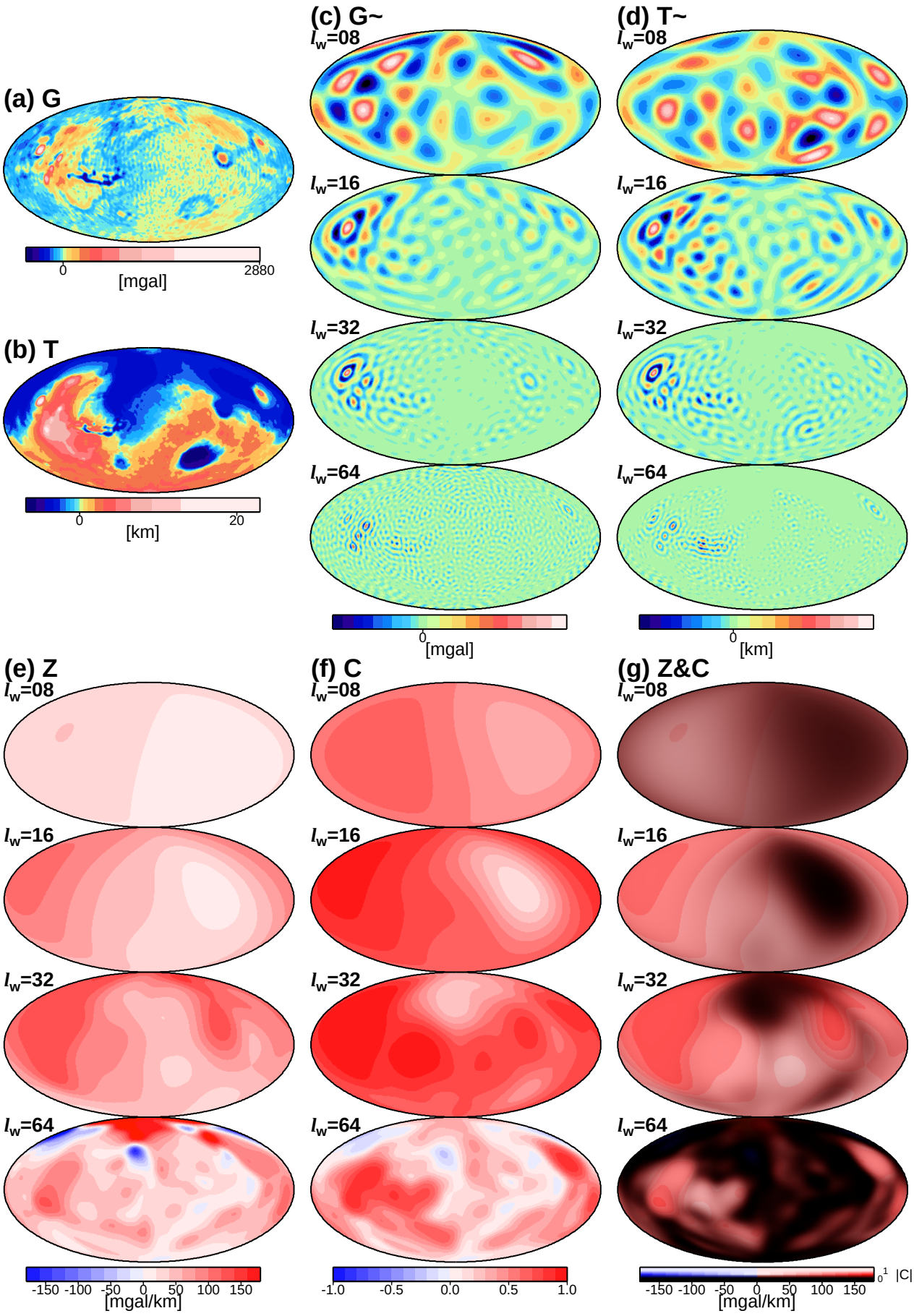
(a) G
0
2880
[mgal]
(b) T
0
20
[km]
(c) G~
l_w=08
l_w=16
l_w=32
l_w=64
0
[mgal]
(d) T~
l_w=08
l_w=16
l_w=32
l_w=64
0
[km]
(e) Z
l_w=08
l_w=16
l_w=32
l_w=64
-150 -100 -50 0 50 100 150
[mgal/km]
(f) C
l_w=08
l_w=16
l_w=32
l_w=64
-1.0 -0.5 0.0 0.5 1.0
(g) Z&C
l_w=08
l_w=16
l_w=32
l_w=64
0 1 |C|
-150 -100 -50 0 50 100 150
[mgal/km]

Fig. 9